Commun. Comput. Phys.
doi: 10.4208/cicp.220111.140711a

Vol. **12**, No. 1, pp. 162-192
July 2012

Efficient Deterministic Modelling of Three-Dimensional Rarefied Gas Flows

V. A. Titarev[1,2,*]

[1] *Dorodnicyn Computing Centre of Russian Academy of Sciences, Vavilov st. 40,
Moscow, Russia, 119333.*
[2] *Cranfield University, Cranfield, UK, MK43 0AL.*

Received 22 January 2011; Accepted (in revised version) 14 July 2011

Communicated by Chi-Wang Shu

Abstract. The paper is devoted to the development of an efficient deterministic framework for modelling of three-dimensional rarefied gas flows on the basis of the numerical solution of the Boltzmann kinetic equation with the model collision integrals. The framework consists of a high-order accurate implicit advection scheme on arbitrary unstructured meshes, the conservative procedure for the calculation of the model collision integral and efficient implementation on parallel machines. The main application area of the suggested methods is micro-scale flows. Performance of the proposed approach is demonstrated on a rarefied gas flow through the finite-length circular pipe. The results show good accuracy of the proposed algorithm across all flow regimes and its high efficiency and excellent parallel scalability for up to 512 cores.

AMS subject classifications: 82D05, 76P05, 82B40, 82C40, 76M12, 65N08, 65B99

Key words: Kinetic, S-model, unstructured, mixed-element, micro channel, rarefied, implicit.

1 Introduction

Past few years have seen rapid development of numerical methods and associated computer codes for solving the Boltzmann kinetic equation with the exact or model collision integrals for three-dimensional problems. The accurate numerical solution of this equation is important in mathematical modelling of gaseous flows inside micro-scale systems, for which popular statistical methods [8] are inefficient. In existing approaches for solving three-dimensional kinetic problems in complex geometries time marching methods are typically used for both steady-state and unsteady calculations, with the only exception reported in [5] for plasma thruster modelling. In [27, 28] a second-order accurate

---

[*] Corresponding author. *Email addresses:* `titarev@ccas.ru`, `titarev@mail.ru` (V. A. Titarev)

structured finite-difference solver for the model kinetic equations was reported. In a series of publications [6, 22, 23] a semi-unstructured Cartesian solver for the Boltzmann equation with both exact and several model collision integrals was developed. Another first-order accurate unstructured-mesh solver was presented [2, 18, 19]. The performance of these methods has been illustrated by computing a number of rarefied gas flows.

Although the above-mentioned methods and associated computer codes represent a significant advance in computational rarefied gas dynamics, there is still much room for improvement. Firstly, the cited three-dimensional methods [2,6,18,19,22,23,27,28] use explicit time evolution with splitting with respect to processes and are thus not efficient for computing steady-state solutions. Existing one- and two-dimensional implicit methods for single-block structured meshes [31, 54, 56] are not easily extendable to complex three-dimensional geometries. Secondly, with the exception [27, 28] their spatial discretization methods do not allow for an accurate and economical resolution for the near-wall layers, which is important in the transitional and near-transitional regime. Thirdly, the scalability of the methods on modern massively parallel clusters has not been properly demonstrated. Since the computational problems associated with the direct numerical solution of the Boltzmann equation are typically large, good parallel performance is very important. Therefore, the development of more effective and universal methods for solving three-dimensional kinetic applications is still an open problem.

The present paper is devoted to the development of a new numerical framework for obtaining three-dimensional solutions of the Boltzmann kinetic equation with the model collision integrals, which circumvents the deficiencies of the existing methods, outlined above. The framework consists of the three main blocks: high-order accurate implicit advection scheme on hybrid unstructured meshes, conservative procedure for the calculation of the model collision integral and a simple and efficient implementation on modern high-performance clusters. The use of unstructured meshes in physical space simplifies the computations in three-dimensional domains of complex geometry and allows for efficient and accurate resolution of near-wall layers. The high-order accurate total variation diminishing (TVD) advection scheme works well for both large Knudsen numbers, when discontinuities of distribution function play an important role, and for moderate and small Knudsen numbers, for which the high order of accuracy is important. The one-step implicit time discretization method accelerates convergence to a steady state by at least an order of magnitude as compared with explicit time evolution methods. Finally, good scalability of the method makes it possible to use relatively fine meshes with moderate computational time required.

The performance of the proposed method is demonstrated on the problem of a rarefied gas flow through a circular micro-scale pipe of finite length driven by pressure difference between the reservoirs attached to the ends of the pipe. The gas flow through a circular orifice (channel of zero length) was studied as early as in 1974 in [38] using a finite-difference method. More recently, flow through a finite-length tube was studied on the basis of the statistical modelling techniques [52]. In the present work the gas flow in the finite-length tube with length to diameter ratio of 10 is used as a relevant computational problem to analyze the performance of the developed method in the wide range of flow regimes. The numerical solution is computed for both small and large pressure jumps using the linearised and non-linear formulations of the kinetic equation, respectively. The calculations are carried out on the basis of S-model kinetic equation [34, 35], but other kinetic models can be easily incorporated. For each case the mass flow rate through the channel is calculated for a wide range of the Knudsen numbers. The three-dimensional results are compared with the asymptotic Poiseuille solution, which corresponds to the assumption of the infinitely long tube. The results include estimates of accuracy, demonstration of the gains of the efficiency due to the implicit time marching as well as the analysis of parallel scalability.

The rest of the paper is organized as follows. In Section 2 the formulation of the test problem and the governing equations are presented, including the non-linear, linearised and Poiseuille formulations. In Section 3 the general method of solution is outlined. Computational results are presented in Section 4. Conclusions are drawn in Section 5.

2 Formulation of the problem

Consider two three-dimensional reservoirs (volumes) filled with the same monatomic gas and connected by a microchannel (tube) of length $2l$ and circular cross section of radius a. Inside the reservoirs away from the channel the gas is at rest with pressures $p_1 > p_2$, respectively, and the same temperature T_0. It is assumed that reservoirs are significantly larger than the micro channel and the gas is in equilibrium far away from the ends of the latter. The actual form and size of reservoirs are thus of no importance. The complete accommodation of momentum and energy of molecules occurs at the channel surface, which is kept under the same constant temperature T_0. The positive pressure difference $\Delta P = p_1 - p_2$ between reservoirs causes the gas movement through the connecting channel. The main quantity of interest is the resulting mass flux through the channel as the function of the pressure difference and degree of gas rarefaction.

Below only channels with $l/a = 10$ are considered. Let us introduce a Cartesian coordinate system (x,y,z) with the centre located in the middle of the channel $x = y = z = 0$ and the Oz axes directed along the channel. Due to the spatial symmetry of the problem only quarter of the spatial domain needs to be considered. The sketch of the resulting flow domain for the circular channel is presented in Fig. 1 with reservoirs schematically shown to be of cylindrical shape. The non-dimensional mass flow rate M to be calculated is given in terms of dimensional gas density ρ and z component of velocity w as

$$M = \frac{\sqrt{2RT_0}}{p_0|A|}\int_A \rho(x,y,z)w(x,y,z)dxdy, \quad p_0 = \frac{1}{2}(p_1 + p_2), \quad -l \le z \le l, \tag{2.1}$$

where A is the cross-sectional area; for the domain shown on Fig. 1 it is equal to $\pi a^2/4$. Note, that mass flow rate M is constant along the channel.

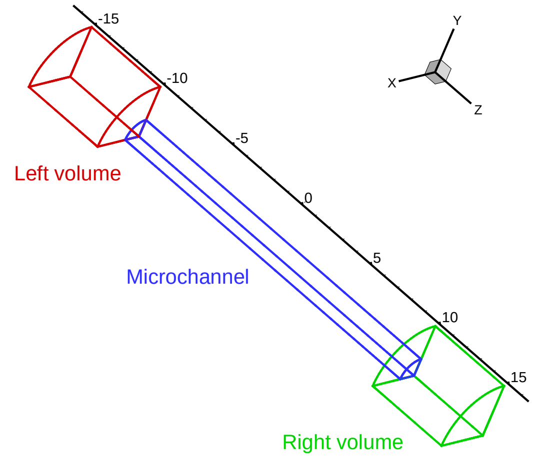

Figure 1: Geometry of the micro channel and reservoirs (volumes) for circular cross section.

2.1 S-model kinetic equation

A steady three-dimensional state of the rarefied gas is determined by the velocity distribution function $f(\boldsymbol{x},\boldsymbol{\xi})$, where $\boldsymbol{x}=(x_1,x_2,x_3)=(x,y,z)$ is the spatial coordinate, $\boldsymbol{\xi}=(\xi_x,\xi_y,\xi_z)$ is the molecular velocity vector. For the rest of the paper, the non-dimensional formulation is used, in which spatial coordinates $\boldsymbol{x}$, mean velocity $\boldsymbol{u}=(u,v,w)=(u_1,u_2,u_3)$, number density n, temperature T, heat flux vector $\boldsymbol{q}=(q_1,q_2,q_3)$ and viscosity μ are scaled using the following quantities:

$$a, \quad \sqrt{2RT_0}, \quad n_0, \quad T_0, \quad mn_0(2RT_0)^{3/2}, \quad \frac{5}{16}mn_0\sqrt{2\pi RT_0}\lambda_0.$$

Here $n_0=p_0/mRT_0$ is the average number density, λ_0 is the mean free path, corresponding to n_0, T_0. Below, the non-dimensional variables are denoted by the same letters as the dimensional ones.

The distribution function f is assumed to satisfy the Boltzmann equation with the S-model collision integral [34,35], which is widely used in calculating micro-channel gas flows, see e.g. [41,42] for a review of the recent results. In the non-dimensional variables the equation takes the form

$$\xi_x\frac{\partial f}{\partial x}+\xi_y\frac{\partial f}{\partial y}+\xi_z\frac{\partial f}{\partial z}=\nu(f^{(S)}-f), \qquad \nu=\frac{8}{5\sqrt{\pi}}\frac{nT}{\mu}\frac{1}{\mathrm{Kn}}, \tag{2.2a}$$

$$f^{(S)}=f_M\left[1+\frac{4}{5}(1-\mathrm{Pr})\boldsymbol{Sc}\left(c^2-\frac{5}{2}\right)\right], \quad f_M=\frac{n}{(\pi T)^{3/2}}\exp\left(-c^2\right), \tag{2.2b}$$

$$v_i=\xi_i-u_i, \qquad c_i=\frac{v_i}{\sqrt{T}}, \qquad S_i=\frac{2q_i}{nT^{3/2}}. \tag{2.2c}$$

Here the Knudsen number $\mathrm{Kn}=\lambda_0/a$ defines the degree of gas rarefaction; for a monatomic gas the Prandtl number $\mathrm{Pr}=2/3$. The non-dimensional gas viscosity is related to gas temperature as $\mu=\sqrt{T}$, which corresponds to the hard-sphere intermolecular interaction. The non-dimensional macroscopic quantities are defined as the integrals of the velocity distribution function with respect to the molecular velocity:

$$\begin{pmatrix} n \\ n\boldsymbol{u} \\ n(\frac{3}{2}T+u^2) \\ \boldsymbol{q} \end{pmatrix} = \int \begin{pmatrix} 1 \\ \boldsymbol{\xi} \\ \xi^2 \\ \frac{1}{2}\boldsymbol{v}v^2 \end{pmatrix} f d\boldsymbol{\xi}. \tag{2.3}$$

The non-dimensional pressure is given by $p=nT$.

The kinetic equation (2.2) has to be augmented with the boundary conditions on the channel and reservoir walls. Let $\boldsymbol{n}=(n_x,n_y,n_y)$ be the inward unit normal vector to a boundary surface. The condition of diffuse molecular scattering on the channel surface with complete thermal accommodation to the surface temperature T_0 is given by:

$$f(\boldsymbol{x},\boldsymbol{\xi})=f_w=\frac{n_w}{(\pi T_0)^{3/2}}\exp\left(-\frac{\xi^2}{T_0}\right), \quad \xi_n=(\boldsymbol{\xi},\mathbf{n})>0. \tag{2.4}$$

The density of reflected molecules n_w is found from impermeability condition stating that the mass flux through the walls is equal to zero:

$$n_w=N_i/N_r, \quad N_i=-\int\limits_{\xi_n<0}\xi_n f d\boldsymbol{\xi}, \quad N_r=+\int\limits_{\xi_n>0}\xi_n\frac{1}{(\pi T_0)^{3/2}}\exp\left(-\frac{\xi^2}{T_0}\right)d\boldsymbol{\xi}. \tag{2.5}$$

The same condition (2.5) is used for the parts of the reservoir walls directly adjacent to the micro channel; these are located at $z=\pm l$. At the rest of the reservoir wall the distribution function of the incoming molecules $\xi_n>0$ is specified as

$$f=f_1=\frac{n_1}{(\pi T_0)^{3/2}}\exp(-\xi^2/T_0), \quad z\to-\infty, \tag{2.6a}$$

$$f=f_2=\frac{n_2}{(\pi T_0)^{3/2}}\exp(-\xi^2/T_0), \quad z\to+\infty. \tag{2.6b}$$

Boundary condition (2.6) is essentially an evaporation boundary condition for the molecules entering the flow domain and is meant to model the indefinitely large reservoirs.

On the symmetry planes $Y0Z$ and $X0Z$ the reflective boundary condition is applied. The distribution function $f_w(\boldsymbol{\xi})$ of the molecules moving from these planes inside the flow domain is given by

$$f_w(\boldsymbol{\xi})=f(\boldsymbol{\xi}'), \quad \boldsymbol{\xi}'=\boldsymbol{\xi}-2\xi_n\boldsymbol{n}, \quad \xi_n\geq 0. \tag{2.7}$$

The expression for the non-dimensional mass flow rate (2.1) takes the form

$$M=\frac{2}{|A|}\int\limits_A \rho w dx dy. \tag{2.8}$$

The two-dimensional integral (2.8) can be calculated at any position z inside the micro channel.

2.2 Linearised kinetic equation

The nonlinear kinetic equation (2.2) is valid for arbitrary ratios of pressures in reservoirs. However, if the pressure difference between reservoirs is small:

$$\frac{|\Delta P|}{p_0} \ll 1.$$

the problem can be simplified by linearizing the distribution function f around the Maxwellian distribution f_0 corresponding to average values of density and temperature n_0, T_0:

$$f = f_0(1+h), \qquad h = h(\boldsymbol{x},\boldsymbol{\xi}), \qquad |h| \ll 1, \tag{2.9a}$$

$$f_0 = \frac{n_0}{(\pi T_0)^{3/2}} \exp(-\xi^2/T_0) \equiv \frac{1}{\pi^{3/2}} \exp(-\xi^2). \tag{2.9b}$$

The deviation of density $\hat{n} = n - n_0$ and temperature $\hat{T} = T - T_0$ from the average values as well as gas velocity $\boldsymbol{u}$ and heat flux $\boldsymbol{q}$ can be expressed via the perturbation h as:

$$\hat{n} = \int f_0 h d\boldsymbol{\xi}, \qquad \boldsymbol{u} = \int \boldsymbol{\xi} f_0 h d\boldsymbol{\xi}, \tag{2.10a}$$

$$\frac{3}{2}(\hat{n} + \hat{T}) = \int \xi^2 f_0 h d\boldsymbol{\xi}, \qquad \boldsymbol{q} = -\frac{5}{4}\boldsymbol{u} + \frac{1}{2}\int \boldsymbol{\xi}\xi^2 f_0 h d\boldsymbol{\xi}. \tag{2.10b}$$

The evolution equation for the perturbation function h is obtained by first inserting (2.9) in the nonlinear kinetic equation (2.2) and then using the assumption $|h| \ll 1$. The resulting linearised equation has the same form as (2.2), but differs by the constant collision frequency ν_0 and the function $h^{(S)}$ in the model collision integral in place of ν and $f^{(S)}$:

$$\xi_x \frac{\partial h}{\partial x} + \xi_y \frac{\partial h}{\partial y} + \xi_z \frac{\partial h}{\partial z} = \nu_0 (h^{(S)} - h), \qquad \nu_0 = \frac{8}{5\sqrt{\pi}} \frac{1}{\mathrm{Kn}}, \tag{2.11a}$$

$$h^{(S)} = \hat{n} + 2\boldsymbol{u}\boldsymbol{\xi} + (\xi^2 - \frac{3}{2})\hat{T} + \frac{8}{5}(1 - \mathrm{Pr})(\xi^2 - \frac{5}{2})\boldsymbol{q}\boldsymbol{\xi}. \tag{2.11b}$$

It is worth noting that in the linearised problem the average quantities become $\hat{p}_0 = \hat{n}_0 = \hat{T}_0 = 0$. The values of pressure inside the reservoirs at $|z| \to \infty$ can thus be expressed as $p_{1,2} = \pm \Delta P$. The boundary conditions in the reservoirs (2.6) in terms of the perturbation function h are given by

$$h = h_1 = +\frac{1}{2}\Delta P, \qquad z \to -\infty,$$

$$h = h_2 = -\frac{1}{2}\Delta P, \qquad z \to +\infty.$$

The boundary condition on the surfaces is obtained by performing the linearization of (2.4), (2.5) and reads as follows:

$$h = h_w, \qquad (\boldsymbol{\xi}, \mathbf{n}) > 0, \qquad h_w = \hat{n}_w, \tag{2.12}$$

where $\hat{n}_w$ is calculated as

$$\hat{n}_w = N_i/N_r, \qquad N_r = \int\limits_{\xi_n>0} \xi_n f_0 d\boldsymbol{\xi}, \qquad N_i = -\int\limits_{\xi_n<0} \xi_n f_0 h d\boldsymbol{\xi}. \tag{2.13}$$

The reflective boundary conditions (2.7) remains unchanged.

The expression for the non-dimensional mass flow rate (2.1) takes the form

$$M = \frac{2}{|A|}\int\limits_A w dx dy. \tag{2.14}$$

2.3 Poiseuille-type flow

Further simplification of the problem can be made if the channel length is assumed to be infinite ($l=\infty$) so that the end effects can be neglected [41]. The gas flow is caused by constant pressure gradient K_p acting along the channel axis, here z axis. The distribution function is then linearized in a way similar to (2.9), but with the perturbation function ψ depending on x and y spatial coordinates only:

$$f = f_0(1+\psi), \quad |\psi(x,y,\boldsymbol{\xi})| \ll 1.$$

The linearized S-model kinetic equation describing the resulting Poiseuille flow is given by [41,51]:

$$\xi_x \frac{\partial\psi}{\partial x} + \xi_y \frac{\partial\psi}{\partial y} = \nu_0(\psi^{(S)} - \psi) + K_p \xi_z, \qquad \psi^{(S)} = 2\xi_z w + \frac{8}{5}(1-\mathrm{Pr}) q_z \xi_z (\xi^2 - \frac{5}{2}). \tag{2.15}$$

The derivation of (2.15) is omitted and can be found in the cited references. Note, that the new linearised equation (2.15) contains a source term, proportional to the acting pressure gradient along the channel. Gas velocity and heat flux are calculated from the perturbation ψ as

$$u_z = \int \xi_z f_0 \psi d_{\text{¸}}, \qquad q_z = \frac{1}{2}\int \xi_z \left(\xi^2 - \frac{5}{2}\right) f_0 \psi d\boldsymbol{\xi}.$$

The problem can be further simplified by integrating with respect to ξ_z; details are omitted. The mass flow rate through the channel is given by the same formula as for the three-dimensional linearised solution (2.14). However, in the case of Poiseuille-type flow (2.15) the perturbation function and thus mass flow rate are linearly proportional to the prescribed pressure gradient K_p. Therefore, the mass flow rate M can be decomposed as

$$M = -K_P M_{\mathrm{Pois}}, \tag{2.16}$$

where the coefficient $M_{\mathrm{Pois}} > 0$ represents the mass flow rate due to the unit pressure gradient. Its value is found by solving (2.15) with $K_P = 1$.

3 Method of solution

The present work describes a computational framework for obtaining numerical solutions of both nonlinear (2.2) and linearised (2.11) three-dimensional kinetic equations. The framework consists of the three main parts: high-order accurate implicit advection scheme on hybrid unstructured meshes based on [49], conservative procedure for the calculation of the model collision integral [45–47] and a simple implementation on modern high-performance clusters. The resulting method and software work across all flow regimes from free-molecular to continuum and allow modelling of rarefied flows in arbitrary-shaped geometries. Below each part of the framework is described in detail.

3.1 Conservative discrete velocity framework

The steady-state solution is found by means of the implicit time-marching algorithm for the kinetic equation in the non-stationary form. Both non-linear (2.2) and linearized (2.11) kinetic equations can be written in the same form as

$$\frac{\partial}{\partial t}g=-\boldsymbol{\xi}\nabla g+J(g),\qquad J=\nu(g^{(S)}-g),\tag{3.1}$$

where g is the distribution function f for the nonlinear case and perturbation h in the linearised case, ∇ is the gradient operator in the physical space (x,y,z); the collision frequency for the linearised model is $\nu\equiv\nu_0$.

The first step in the numerical solution procedure is to replace the infinite domain of integration in the molecular velocity space $\boldsymbol{\xi}$ by a finite computational domain $|\xi_x|,|\xi_y|,|\xi_z|\le\xi_0$, which is then discretized using the non-uniform Cartesian mesh with $N_{\xi_x}\cdot N_{\xi_y}\cdot N_{\xi_z}\equiv N_\xi$ cells. The velocity distribution function is then defined in centers $\boldsymbol{\xi}_\alpha$ of the resulting velocity mesh so that $g_\alpha=g(\boldsymbol{x},\boldsymbol{\xi}_\alpha)$. The kinetic equation (3.1) is replaced by a system of N_ξ advection equations for each of g_α:

$$\frac{\partial}{\partial t}g_\alpha=-\boldsymbol{\xi}_\alpha\nabla g_\alpha+J(g_\alpha),\tag{3.2}$$

which are connected by the macroscopic parameters in the function $g^{(S)}$ from the model collision integral J.

The description of the method (3.2) is complete once the calculation of the model collision integral and the advection scheme are described.

3.2 Approximation of the model collision integral

The evaluation of the model collision integral in the right-hand side of (3.2) requires the knowledge of eight macroscopic quantities, namely, the density, temperature, velocity and heat flux vectors. These are to be computed from the values of the distribution function g_α in the molecular velocity cells $\boldsymbol{\xi}_\alpha$. The direct approximation of the expressions for these quantities yields a non-conservative numerical method that violates the discrete mass, momentum, and energy conservation laws [47]. As a result, the computation of the flow at small Knudsen numbers becomes difficult. A numerical illustration of this can be found in [47].

There are several such methods for model kinetic equations in the current literature. In [11] the author mentions a conservative algorithm to calculate macroscopic quantities in one space dimension based on conservation laws, although no details are given. In [14, 25] a correction procedure for the function $f^{(S)}$ in the model collision integral was proposed which is applicable to various monatomic and diatomic kinetic models. Another method for the BGK equation [7] is based on minimization of the entropy in the discretized molecular velocity space [31, 32] and essentially results in a system of equations for density, velocity and temperature based on conservation laws only. It is shown that the resulting numerical method for the BGK equation satisfies the conservation laws and the entropy dissipation. See also [16]. However, it is unclear if the method [31, 32] can be extended to models for which the H theorem has not yet been proven, such as monatomic model of Shakhov [35, 35] (used in the present study) and diatomic model of Rykov [26, 33]. For these models the use of the conservation laws alone is not sufficient since the heat flux vector remains undefined.

The present work uses the most recent approach [45–47], which has been successfully applied to all above-mentioned models. Its key idea can be explained as follows. Since the differential parts of the exact and model kinetic equations are the same, one requires that first few moments of exact collision integral $I(f,f)$ coincide with the first few moments of the model collision integral $J(f,\boldsymbol{a},\boldsymbol{\xi})$:

$$\int \phi(\xi) J(f,\boldsymbol{a},\xi) d\boldsymbol{\xi} = \int \phi(\xi) I(f,f) d\boldsymbol{\xi}, \quad \phi(\xi) = 1,\ \xi_i,\ \xi^2,\ \xi_i\xi_j,\ \xi_i\xi_j\xi_k, \cdots. \tag{3.3}$$

Here the unknown parameter vector $\boldsymbol{a}$ depends on the chosen model equation. It is further assumed that the approximation conditions (3.3) should be satisfied for the Maxwellian molecules only. Then the moments of the exact collision integral can be evaluated analytically and the vector $\boldsymbol{a}$ turns out to be the vector of macroscopic quantities, which are expressed via the integrals of the velocity distribution function, e.g. for the S-model equation one obtains (2.3). A conventional numerical approach is then to approximate these expressions by a numerical quadrature rule. However, this leads to the non-conservative approximations caused by integration errors in velocity space.

To make the method conservative with the respect to the collision integral, it was suggested in [45–47] to discretise (3.3) directly and solve the resulting nonlinear system of equations for macroscopic quantities $\boldsymbol{a}$. Obviously, such method does not need the H theorem and can be applied to any kinetic model. In case of monatomic model of Shakhov [35, 35] the use of (3.3) results in eight equations for gas number density, temperature, three components of velocity and three components of the heat flux. In case of the diatomic model of Rykov [33] there are six conservation equations and six additional equations representing relaxation of translational and rotational heat fluxes. For both models the method thus not only ensures conservation with respect to the model collision integral, but also guaranties the correct relaxation of heat fluxes.

3.2.1 Nonlinear kinetic model

Let ω_α be the weights of the second order composite quadrature rule used for integration in $\boldsymbol{\xi}$ space. For the nonlinear model ($g\equiv f$) in order to compute the vector of primitive variables

$$\boldsymbol{W}=(n,u_1,u_2,u_3,T,q_1,q_2,q_3)^T$$

for each spatial cell the conservative procedure for the calculation of the macroscopic quantities [45–47] gives the following system of equations

$$\boldsymbol{R}=\sum_\alpha \begin{pmatrix} 1 \\ \boldsymbol{\xi} \\ \xi^2 \\ \boldsymbol{v}v^2 \end{pmatrix}_\alpha (f^{(S)}_\alpha - f_\alpha)\omega_\alpha + \begin{pmatrix} 0 \\ \boldsymbol{0} \\ 0 \\ 2\mathrm{Pr}\boldsymbol{q} \end{pmatrix} = \boldsymbol{0}. \tag{3.4}$$

Here subscripts i are n are omitted for simplicity. The eight equations (3.4) are solved using the Newton iterations the initial guess for which is provided by the direct (non-conservative) approximation for (2.3)

$$\begin{pmatrix} n \\ n\boldsymbol{u} \\ \frac{3}{2}nT+n\boldsymbol{u}^2 \\ \boldsymbol{q} \end{pmatrix} = \sum_\alpha \begin{pmatrix} 1 \\ \boldsymbol{\xi} \\ \xi^2 \\ \frac{1}{2}\boldsymbol{v}v^2 \end{pmatrix}_\alpha f_\alpha\omega_\alpha.$$

Usually, one or two Newton iterations are sufficient for convergence. In the special case $\mathrm{Pr}=1$ (BGK model [7]) the function $f^{(S)}$ no longer contains the heat flux vector making last three equations for the heat flux in (3.4) not necessary. As a result, the procedure (3.4) for macroscopic parameters coincide with the ones proposed in [31,32].

3.2.2 Linearised kinetic model

For the linearised model ($g\equiv h$) the conditions (3.4) are simplified into the following equations:

$$\int \begin{pmatrix} 1 \\ \boldsymbol{\xi} \\ \xi^2 \\ \boldsymbol{\xi}\xi^2 \end{pmatrix} f_0(h^{(S)}-h)d\boldsymbol{\xi} + \begin{pmatrix} 0 \\ \boldsymbol{0} \\ 0 \\ 2\mathrm{Pr}\boldsymbol{q} \end{pmatrix} = \boldsymbol{0}. \tag{3.5}$$

When re-written in the discrete form as

$$\sum_\alpha \begin{pmatrix} 1 \\ \boldsymbol{\xi}_\alpha \\ \xi^2_\alpha \\ \boldsymbol{\xi}_\alpha\xi^2_\alpha \end{pmatrix} f_{0,\alpha}h^{(S)}_\alpha\omega_\alpha + \begin{pmatrix} 0 \\ \boldsymbol{0} \\ 0 \\ 2\mathrm{Pr}\boldsymbol{q} \end{pmatrix} = \boldsymbol{b}, \quad \boldsymbol{b}=\sum_\alpha \begin{pmatrix} 1 \\ \boldsymbol{\xi}_\alpha \\ \xi^2_\alpha \\ \boldsymbol{\xi}_\alpha\xi^2_\alpha \end{pmatrix} f_{0,\alpha}h_\alpha\omega_\alpha,$$

it represents a linear system

$$H\hat{\boldsymbol{W}}=\boldsymbol{b}, \tag{3.6}$$

for the vector of the primitive variables

$$\hat{\boldsymbol{W}}=(\hat{n},u_1,u_2,u_3,\hat{T},q_1,q_2,q_3)^T.$$

No iteration is required to compute the macroscopic quantities. It should be noted that system (3.6) is new. The constant matrix H has the size 8×8 and is computed numerically using the same quadrature rule as for the macroscopic quantities. It is inverted and stored in computer memory at the beginning of time marching. The vector $\boldsymbol{b}$ of integrals of the function h in the right hand side is recalculated every time step.

3.3 Advection scheme

3.3.1 Framework

The next step is to describe a numerical method to solve each of the kinetic equations (3.2) assuming the model collision integral is known. The method used in the present work is a further evolution of unstructured-mesh solvers developed in a sequence of papers [48–51]. Introduce in the physical variables $\boldsymbol{x}=(x_1,x_2,x_3)=(x,y,z)$ a computational mesh consisting of prismatic and hexahedral elements (spatial cells) V_i. The total number of spatial cells is N_{space}. Also denote by $|V_i|$ the cell volume, $|A|_{il}$ area of face l. Let $\Delta t= t^{n+1}-t^n$, $g^n_\alpha=g(t^n,\boldsymbol{x},\boldsymbol{\xi}_\alpha)$, $\delta^n_\alpha=g^{n+1}_\alpha-g^n_\alpha$. The implicit one-step method for the kinetic equation (3.2) has the following form:

$$(1+\Delta t\nu^n+\Delta t\boldsymbol{\xi}_\alpha\nabla)\delta^n_\alpha=\Delta t L^n_\alpha, \qquad L^n_\alpha=-\boldsymbol{\xi}_\alpha\nabla g^n_\alpha+J^n_\alpha. \tag{3.7}$$

Compared to a typical explicit method, the left-hand side of (3.7) contains two additional terms. The advection term $\Delta t\boldsymbol{\xi}_\alpha\nabla$ may be viewed as an extension to the unstructured-mesh case the implicit two-dimensional structured solvers from [17,54]. The second term $\Delta t\nu^n$ corresponds to the semi-implicit approximation of the loss term $(-\nu g)$ in the model collision integral and explicit treatment of the gain term $\nu g^{(S)}$. This approach to the implicit treatment of the model collision integral has been routinely used in the steady-state iterative solvers, see e.g. [3,36,37,43]. It appears that in the time-marching methods such treatment was first used in [54] in the context of a single-block structured solver. It is also possible to consider the implicit treatment of $g^{(S)}$ as was done in [31,32] for the two-dimensional BGK model. However, such approach results in a much more complicated numerical scheme, which is also difficult to implement on shared-memory machines, and is thus not used here.

In order to pass from the differential form (3.7) to the fully discrete scheme, spatial integration over the cell V_i is carried out. The advection operator in the left-hand side of (3.7) is discretized with first-order upwind spatial differences whereas the right-hand side L^n_α is approximated using a second-order non-oscillatory method. Let $g^n_{\alpha i}$ be the spatial average of the velocity distribution function in the cell V_i at time t^n for the molecular velocity $\boldsymbol{\xi}_\alpha$. Let $\sigma_l(i)$ be the cell index of the cell adjacent to the face l of cell V_i. Then for the given α the implicit finite-volume method based on (3.7) takes the form of a system of N_{space} linear equations for $g^n_{\alpha i}$:

$$(1+\nu_i^n\Delta t)\delta^n_{\alpha i}+\frac{\Delta t}{|V_i|}\sum_l \xi_{\alpha nl}F_l(\delta^n_{\alpha i},\delta^n_{\sigma_l(i)})|A_{il}|=\Delta t L^n_{\alpha i}, \tag{3.8a}$$

$$\delta^n_{\alpha i}=g^{n+1}_{\alpha i}-g^n_{\alpha i},\qquad L^n_{\alpha i}=-(\boldsymbol{\xi}_\alpha\nabla g^n_\alpha)_i+J^n_{\alpha i}, \tag{3.8b}$$

where $\xi_{\alpha nl}$ is the projection of the vector $\boldsymbol{\xi}_\alpha$ onto the unit normal to the face l of the cell V_i. The quantity F_l in the left-hand side of the method corresponds to the upwind first-order accurate approximation of the advection operator and is given by

$$F_l=\frac{1}{2}(\delta^n_{\alpha i}+\delta^n_{\alpha,\sigma_l(i)})-\frac{1}{2}\mathrm{sign}(\xi_{\alpha nl})\cdot(\delta^n_{\alpha,\sigma_l(i)}-\delta^n_{\alpha i}),$$

if the face l of the cell V_i is adjacent to a computational boundary (either wall, reflection or inflow/outflow), the corresponding value $\delta^n_{\alpha,\sigma_l(i)}=0$. In the right-hand side of the scheme the advection operator acting on the values of the velocity distribution function on the lower time level, is approximated as a sum of fluxes through cell sides:

$$(\boldsymbol{\xi}_\alpha\nabla g^n_\alpha)_i=\frac{1}{|V_i|}\sum_l \Phi^n_{\alpha il}, \tag{3.9a}$$

$$\Phi^n_{\alpha il}=\frac{1}{2}\xi_{\alpha nl}|A_{il}|\left(g^-+g^+-\mathrm{sign}(\xi_{\alpha nl})(g^+-g^-)\right), \tag{3.9b}$$

$$g^-=g^n_{\alpha il},\qquad g^+=g^n_{\alpha,\sigma_l(i),l_1}. \tag{3.9c}$$

Here l_1 is the number of the face of the cell $\sigma_l(i)$, adjacent to the face l of the cell i, the face averages $g^n_{\alpha il}$ of the function g for each cell i are computed to high order of accuracy by means of the reconstruction procedure, described in the next section.

The general formula (3.9) is modified if the face l is adjacent to a solid boundary and $\xi_{\alpha nl}<0$ by applying the boundary condition:

$$\Phi^n_{\alpha il}=\xi_{\alpha nl}g_w|A_{il}|.$$

In particular, the boundary condition of diffuse reflection (2.4), (2.5) is approximated in such a way as to satisfy the impermeability condition exactly. Define

$$G=\sum_{\xi_{\alpha nl}\le 0}\xi_{\alpha nl}f_{0,\alpha}\omega_\alpha,\qquad f_{0,\alpha}=(\pi T_0)^{-3/2}e^{-\xi_\alpha^2/T_0}.$$

For the nonlinear kinetic model (2.2) the density of the reflected molecules in (2.5) for the face l of the cell V_i is computed as

$$(n_w)_{il}=-\frac{1}{G}\sum_{\xi_{\alpha nl}>0}\xi_{\alpha nl}f^n_{\alpha il}\omega_\alpha. \tag{3.10}$$

For the linearized equation (2.11) the corresponding expression takes (2.13) the form

$$(n_w)_{il} = -\frac{1}{G}\sum_{\xi_{\alpha nl}>0} \xi_{\alpha nl} h^n_{\alpha il} f_{0,\alpha}\omega_\alpha. \tag{3.11}$$

Another type of the boundary condition is that of the specular reflection (2.7) and is approximated in a straightforward manner owing to the Cartesian orientation of the reflection planes.

The description of the advection scheme is complete (3.8) once methods to compute the numerical fluxes $\Phi^n_{\alpha il}$ and the temporal increments of the distribution function $\delta_{\alpha i}$ are provided. The calculation of the model collision integral $J_{\alpha i}$ has already been described in Section 3.2.

3.3.2 Spatial reconstruction procedure

The calculation of the numerical fluxes $\Phi^n_{\alpha il}$ with high-order of accuracy requires the knowledge of the face averages of the distribution function $g^n_{\alpha il}$. For the first-order accurate method it is sufficient to set these face values equal to the cell value $g^n_{\alpha il} = g^n_{\alpha i}$. It is well known, however, that the first-order method is quite inaccurate. In particular, for kinetic equations first-order spatial approximation leads to highly inaccurate results for transitional and nearly-continuum flow regimes; examples can be found in e.g. [50]. In the present method a piece-wise linear reconstruction of the solution in each spatial cell is used, leading to the second-order accurate face values of the distribution function and consequently second-order accurate spatial discretization method. The details of the reconstruction procedure are outlined below.

In each spatial cell V_i the distribution function g_α is approximated locally by the reconstruction polynomial. The coefficients of the polynomial are computed using the values of g in the cell V_i and a sufficient number of its neighbours, which form the so-called spatial reconstruction stencil. For convenience, let us introduce for each cell V_i a local numbering of cells with the index $m = 0,1,\cdots$; the cell V_i is referred to as V_{i0}, whereas the rest of the cells from the stencil are named V_{im}, $m = 1,\cdots M_i$. Here M_i is the total number of cells in the stencil, different from the cell V_i. Correspondingly, the values of the distribution function in these cells are named $g^n_{\alpha im}$, with $g^n_{\alpha i0} \equiv g^n_{\alpha i}$. The aim is then to have a method to form the piece-wise linear approximation of g inside V_i from cell-averaged values $g^n_{\alpha im}$.

The reconstruction procedure can be carried out in the physical space (x,y,z). The reconstruction stencil is constructed by adding a sufficient number of cells to the first cell V_i, starting with direct neighbours and then if necessary neighbours of the direct neighbours. Fig. 2 shows a typical reconstruction stencil around a hexahedral cell near the channel's surface in the physical coordinate system (x,y,z). The stencil consists of six hexahedral cells and one prismatic cell. There is an evident stretching in one coordinate direction due to the mesh clustering towards the channel surface. On the other hand, in another coordinate direction the cell dimensions are quite large — this is the direction along the channel, z coordinate direction. The scaling effects associated with such

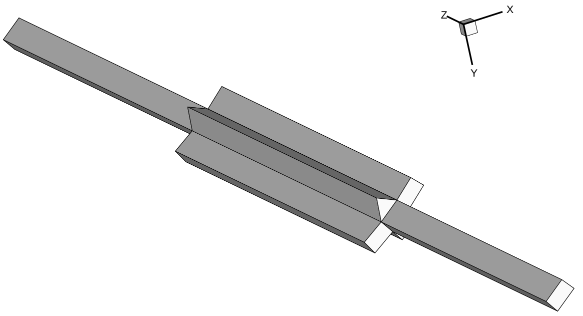

Figure 2: Reconstruction stencil in the physical coordinate system (x,y,z) for a hexahedral mesh.

elongated cells or simply with any cells of poor quality can result in badly conditioned reconstruction matrixes and thus low accurate reconstruction. However, the use of elongated hexahedral or prismatic cells is essential for modelling of flows in long channel as it allows to reduce the total number of spatial cells and cannot thus be avoided.

In order to remove scaling effects, the reconstruction is carried out in the local coordinate system [9]. Let (x_k,y_k,z_k), $k=1,\cdots 4$ be the coordinates of some four vertexes of the cell V_i. The coordinate transformation from the global coordinate system to the local one $\hat{\boldsymbol{x}}=(\hat{x},\hat{y},\hat{z})$ is then defined as

$$\begin{pmatrix} x \\ y \\ z \end{pmatrix} = \begin{pmatrix} x_1 \\ y_1 \\ z_1 \end{pmatrix} + J_i \begin{pmatrix} \hat{x} \\ \hat{y} \\ \hat{z} \end{pmatrix}, \qquad J_i = \begin{bmatrix} x_2-x_1 & x_3-x_1 & x_4-x_1 \\ y_2-y_1 & y_3-y_1 & y_4-y_1 \\ z_2-z_1 & z_3-z_1 & z_4-z_1 \end{bmatrix}. \tag{3.12}$$

The reconstruction stencil in the local coordinate system is obtained by applying the inverse transformation (3.12) from $\boldsymbol{x}$ to $\hat{\boldsymbol{x}}$ to each cell of the original stencil and consists of the transformed cells V'_{im}, $m=0,\cdots,M$. Fig. 3 shows the resulting of applying this trans-

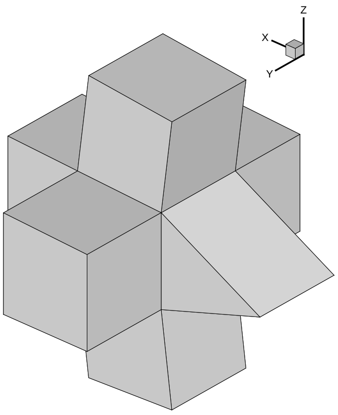

Figure 3: Reconstruction stencil from Fig. 2 in the reference coordinate system $(\hat{x},\hat{y},\hat{z})$.

formation to the stencil shown on Fig. 2. It is obvious that in the reference coordinate system all cells in the stencils are now of similar size and close to unit shapes. The slight curvature of the elements is due to the circular shape of the micro channel followed by the spatial mesh.

The linear reconstruction polynomial $p_{\alpha i}(\hat{x})$ is given by the expansion over the basis functions $e_{ik}(\hat{x})$:

$$p_{\alpha i}(\hat{x}) = g^n_{\alpha i} + \sum_{k=1}^{3} a^n_{\alpha ik} e_{ik}(\hat{x}), \qquad e_{ik} \equiv \hat{x}_k - \frac{1}{|V'_{i0}|} \int_{V'_{i0}} \hat{x}_k d\hat{x}. \tag{3.13}$$

Note, that due to the choice of the basis functions the reconstruction is conservative. To compute the unknown coefficients $a^n_{\alpha ik}$ it is required that for each cell from the stencil the cell average of the reconstruction polynomial be equal to the cell average of the function g:

$$\frac{1}{|V'_{im}|} \int_{V'_{im}} p_{\alpha i}(\hat{x}) d\hat{x} = g^n_{\alpha i0} + \frac{1}{|V'_{im}|} \sum_{k=1}^{3} \int_{V'_{im}} a^n_{\alpha ik} e_{ik} d\hat{x} = g^n_{\alpha im}. \tag{3.14}$$

The calculation of three coefficients $a^n_{\alpha i1}$, $a^n_{\alpha i2}$ and $a^n_{\alpha i3}$ requires at least three equations of the form (3.14). However, on tetrahedral meshes the use of only three cells ($M=3$) results in an unstable scheme [9]. It appears that the same applies to other cells types, such as hexahedral etc. Therefore in the present work the following stencils sizes are used: $M=9$ for tetrahedral and pyramidal cells, $M=5$ for prismatic cells and $M=6$ for hexahedral cells. The resulting over-determined system of linear equations for a_k is solved using the least-square method so that the coefficients of the polynomial can be expressed directly as the linear combination of the values of the distribution function in the stencil:

$$\begin{pmatrix} a^n_{\alpha i1} \\ a^n_{\alpha i2} \\ a^n_{\alpha i3} \end{pmatrix} = D_i \cdot \begin{pmatrix} g^n_{\alpha 00} \\ g^n_{\alpha 01} \\ g^n_{\alpha 02} \\ \cdots \\ g^n_{\alpha 0M_i} \end{pmatrix}, \qquad D_i = \begin{pmatrix} d_{00} & d_{01} & \cdots & d_{0M_i} \\ \cdots & & & \\ d_{30} & d_{31} & \cdots & d_{3M_i} \end{pmatrix}.$$

For the linear second-order method it is sufficient to set face values of the distribution function $g_{\alpha il}$ equal to the face averages $p_{\alpha il}$ of the reconstruction polynomial. These averages are expressed in terms of the polynomial coefficients and face averages of the basis functions e_{ikl} as

$$p_{\alpha il} = g^n_{\alpha i} + \sum_{k=1}^{3} a^n_{\alpha ik} e_{ikl}.$$

Note that in calculations, the constant matrix D_i and face averages of the basis functions e_{ikl} are calculated and stored in memory for each cell V_i before the time marching begins.

It is well known that linear high-order methods are not monotone [13]. In order to eliminate spurious oscillations [20, 21, 24, 44] the reconstruction procedure uses the so-called slope limiter $\psi_{\alpha i}$. This is equivalent to replacing the coefficients $a^n_{\alpha ik}$ by the modified coefficients $\tilde{a}^n_{\alpha ik} = \psi_{\alpha i} a^n_{\alpha ik}$. A good choice of the slope limiter for steady-state calculations is found in [53]. The face-averages of the distribution function g_{il}, used in the actual calculations, are given by

$$g^n_{\alpha il} = g^n_{\alpha i} + \psi_{\alpha i} \cdot (p_{\alpha il} - g^n_{\alpha i}) = g^n_{\alpha i} + \psi_{\alpha i} \cdot \sum_{k=1}^{3} a^n_{\alpha ik} e_{ikl}. \tag{3.15}$$

The first-order scheme is recovered by setting $\psi_{\alpha i} \equiv 0$ whereas $\psi_{\alpha i} \equiv 1$ leads to a linear (oscillatory) spatially second-order method.

The described reconstruction procedure can be extended to polynomial reconstructions of any order of spatial accuracy. However, the test calculations have shown that the piece-wise linear (second-order) representation is the best compromise between the accuracy and computational cost. It appears as if the higher than second order reconstructions should be used in the weighted essentially non-oscillatory (WENO) framework only [9, 10, 55], whereas in the present framework the use of slope limiter affects the performance of the third- and higher-order accurate methods, making them computationally unattractive as compared to the second-order accurate one.

3.3.3 Time evolution

The direct numerical solution of the linear system (3.8) is a very slow operation with the computational cost proportional to N^3_{space}. Therefore, an approximate factorization of the system is carried out using the approach suggested (but not implemented) in [29, 30]. Regrouping of (3.7) yields

$$\delta^n_{\alpha i} + \sum_l \Delta t z_{i,\sigma_l(i)} \delta^n_{\alpha \sigma_l(i)} = \frac{\Delta t}{\lambda_i} L^n_{\alpha i}, \tag{3.16}$$

where the coefficients $z_{i,\sigma_l(i)}$ and λ_i are given by

$$\begin{aligned} &b_{\alpha i} = \sum_l \xi_{\alpha nl} (1 + \mathrm{sign}\xi_{\alpha nl}) \frac{|A_{il}|}{2|V_i|}, \qquad c_{\alpha,i,\sigma_l(i)} = \xi_{\alpha nl}(1 - \mathrm{sign}\xi_{\alpha nl}) \frac{|A_{il}|}{2|V_i|}, \\ &\lambda_{\alpha i} = 1 + \Delta t \nu^n_i + \Delta t b_{\alpha i}, \qquad z_{\alpha i \sigma_l(i)} = \frac{1}{\lambda_{\alpha i}} c_{\alpha i \sigma_l(i)}, \end{aligned}$$

or in the matrix form

$$(I + \Delta t Z_\alpha) \cdot \delta^n_\alpha = \Delta t \Lambda^{-1}_\alpha \cdot \boldsymbol{L}^n_\alpha, \tag{3.17}$$

where

$$\delta_\alpha = \begin{pmatrix} \delta_{\alpha 1} \\ \delta_{\alpha 2} \\ \cdots \\ \delta_{\alpha N_{space}} \end{pmatrix}, \quad \boldsymbol{L}^n_\alpha = \begin{pmatrix} L^n_{\alpha 1} \\ L^n_{\alpha 2} \\ \cdots \\ L^n_{\alpha N_{space}} \end{pmatrix}, \quad \Lambda_\alpha = \begin{pmatrix} \lambda_{\alpha 1} & 0 & \cdots & 0 \\ 0 & \lambda_{\alpha 1} & \cdots & 0 \\ 0 & 0 & \cdots & 0 \\ 0 & 0 & \cdots & \lambda_{\alpha 1} \end{pmatrix}.$$

Next, the matrix Z_α is approximately factorized into the product of a low-triangular L_α and upper-triangular U_α matrices according to the expression

$$l_{ij}=\begin{cases}\Delta t z_{ij}, & j<i,\\ 0, & j>i,\end{cases}\qquad u_{ij}=\begin{cases}0, & j<i,\\ \Delta t z_{ij}, & j>i,\end{cases}\qquad l_{ii}=u_{ii}=1,$$

so that

$$I+\Delta t Z_\alpha = L_\alpha \cdot U_\alpha + \mathcal{O}(\Delta t^2).$$

The implicit method (3.7) takes its final form:

$$L_\alpha \cdot U_\alpha \cdot \delta^n_\alpha = \Delta t \Lambda^{-1}_\alpha \cdot \boldsymbol{L}^n_\alpha, \qquad g^{n+1}_{\alpha i} = g^n_{\alpha i} + \delta^n_{\alpha i}. \tag{3.18}$$

The computational cost of solving (3.18) is linearly proportional to N_{space}. As a result, the cost of one time step of the implicit method is only 25% larger than the computational cost of an explicit method with the same spatial reconstruction procedure and the conservative calculation of macroscopic parameters. If the computer memory allows to store the matrices L, U and Λ from (3.18) rather than recalculate them at each time step, the implicit method becomes practically as fast as the explicit one.

In calculations, the value of the time step Δt is evaluated according to the expression

$$\Delta t = C \min_i d_i / \xi_0,$$

where C is the prescribed CFL number, d_i the characteristic linear size of the cell V_i.

3.4 Convergence criteria

The convergence of the solution to the steady-state is verified by calculating the global residual in the macroscopic conservation laws. For any spatial cell i the local vector residual $\boldsymbol{R}^n_i$ in conservation laws is defined as

$$\boldsymbol{R}^n_i = \sum_\alpha \begin{pmatrix} 1 \\ \boldsymbol{\xi}_\alpha \\ \xi^2_\alpha \end{pmatrix} L^n_{i\alpha} s_\alpha \omega_\alpha,$$

where $s_\alpha \equiv 1$ for the nonlinear kinetic equation (2.2) and $s_\alpha = f_{0,\alpha}$ for the linearized one (2.11). The corresponding global L_0 and L_1 norms of residuals in the conservation laws for time step n are given by

$$E^n_0 = \max_i \sum_i |\boldsymbol{R}^n_i|, \qquad E^n_1 = \frac{1}{|V|}\sum_i |\boldsymbol{R}^n_i|\cdot|V_i|, \qquad |V| = \sum_i |V_i|. \tag{3.19}$$

The numerical solution is deemed as converged to the steady state if

$$E^n_0 \le \epsilon_0, \qquad E^n_1 \le \epsilon_1. \tag{3.20}$$

For single-precision calculations of the present paper the following values of the tolerance parameters are usually applied: $\epsilon_0 = 10^{-3}$, $\epsilon_1 = 10^{-5}$.

It should be noted that for large values of the CFL coefficient C the residual may not drop below a certain value. This is due to the non-smooth behaviour of the slope limiter, which does not depend continuously on the solution. To improve the convergence, the values of the slope limiter are frozen once the L_1 residual drops below 10^{-3}.

3.5 Summary of the sequential algorithm

The calculation of one time step in the single-processor (sequential) version of the method consists of the following stages.

1. Calculation of the polynomial coefficients $a_{\alpha ik}$ and application of the slope limiter $\psi_{\alpha i}$; the resulting values are stored in memory.
2. Calculation of integral sums in the boundary conditions (3.10), (3.11) and evaluation of the density of reflected molecules for all cell faces belonging to boundaries.
3. For each α calculation of the face values (3.15), numerical fluxes (3.9), temporal update (3.7) and addition to integral sums in the steady-state residual calculations (3.19) and for the macroscopic parameters (3.4).
4. The time marching finishes once the convergence condition (3.20) is met.

The memory requirements of the second-order version of the method can be split into two groups: memory for the advection scheme coefficients (such as reconstruction matrix D_i) and memory to store the solution. The memory requirements of the scheme depend on the type of the spatial cells used. For the hexahedral cells the scheme needs approximately 25 integers and 40 reals to store mesh data and 8 integers and 70 reals to store reconstruction data. For the solution for each cell $(\boldsymbol{x}_i, \boldsymbol{\xi}_\alpha)$ of the six-dimensional mesh 5 real numbers need to be stored: value of g, three polynomial coefficients $a_{\alpha ik}$ and value of the slope limiter $\psi_{\alpha i}$. Additionally, for each of N_{space} spatial cell the values of 8 macroscopic quantities and 5 components of the steady residual vector need to be stored. For the non-linear kinetic model some additional quantities also need to be stored. Overall, for sequential runs the solution memory required to store the distribution function accounts for the bulk of the computer memory used in the calculations.

3.6 Parallel implementation

The three-dimensional calculation of rarefied flows requires large computational meshes. A coarse mesh for a single isolated micro channel can contain 10^5 spatial cells and typically 16^3 molecular velocity cells, so that the total number of cells in the six-dimensional computation is at the order of $10^{10} \cdots 10^{11}$. Such meshes put high demands on both computing power and memory, which go beyond the limits of a typical single-processor machine. Therefore, single-processor solutions of such problems cannot be carried out.

In order to circumvent the above-mentioned difficulties, the present numerical algorithm is implemented on multi-core clusters using Message Passing Interface (MPI) programming paradigm [15]. Unlike conventional approaches, in which the spatial mesh (in physical coordinates) is split into blocks (see e.g. [10]), in the present work the decomposition of the ξ_z and ξ_x directions of the rectangular molecular velocity mesh is implemented. The present approach to parallel implementation is similar to the one used earlier for the Boltzmann equation with the exact collision integral [4]. For each block the kinetic equation is solved using the implicit method (3.7). The sequential algorithm is then modified to include inter-processor communications in the calculation of integral sums with respect to the molecular velocity mesh as well as data exchange for the reflective boundary condition (2.7).

The advantages of the present approach to parallelization over existing methods [18, 23] are three-fold. Firstly, it is relatively simple to implement since no spatial domain decomposition is required. Secondly, it retains the main advantage of the implicit method (3.7) — fast convergence to the steady-state solution. Finally, practically ideal load balancing can be achieved since each of the processor will perform exactly the same amount of calculations.

4 Results

The numerical method has been tested by calculating the solution to the problem for various values of the Knudsen number and pressure ratios. The summary of the computed cases is given by Table 1, which lists the boundary data in the reservoirs. All calculations are run on the high-performance computing facility 'Astral' of the Cranfield university, which is a Hewlett Packard machine comprising 856 Intel Woodcrest cores (3.0GHz).

Table 1: Description of test cases.

Pressure ratio	Left reservoir	Right reservoir
Linearized	$\hat{p}_1=1$	$\hat{p}_2=-1$
$p_1/p_2=1.1$	$p_1=1.047619$	$p_2=0.952381$
$p_1/p_2=2$	$p_1=1.333333$	$p_2=0.666667$

In most of the published data the so-called rarefaction parameter is used instead of the Knudsen number. In the present work this parameters coincides with the constant collision frequency ν_0 in the linearized equation (2.11). In order to make it easier for the reader to compare our results with those, published in the literature, below ν_0 is used instead of the Knudsen number Kn. The collision frequency in the full nonlinear S-model equation (2.2) is then related to ν_0 as

$$\nu=\frac{nT}{\mu}\nu_0.$$

The free-molecular regimes corresponds to $\nu_0=0$ whereas the nearly-continuum flow is obtained when $\nu_0 \gg 1$.

4.1 Computational tests

Two sets of calculations have been performed in order to access the efficiency of the implicit time marching as well as scalability properties of the algorithm when used on multi-core systems. These are two key properties of the proposed numerical algorithms, which are specific to the kinetic equation and represent a major improvement over existing methods. The study of the accuracy of the spatial reconstruction scheme and its ability to handle general geometries are not included as it is fairly general method and has been accessed in previous work, e.g. [49].

The first set of calculations is intended to study the influence of the CFL coefficient on the convergence to the steady-state. Two spatial meshes were considered, which are summarized in Table 2. The first spatial mesh is mixed-element and consisted for elements of all types whereas the second mesh is purely hexahedral. A weak clustering towards the surface of the tube was used for both meshes with the cells size of 0.04 normal to the surface. Figs. 4-7 show the details of the spatial distribution of cells in both cases. The molecular velocity mesh contained 16^3 cells with uniform spacing. The total number of cells is thus $\approx 2\times 10^8$.

Table 2: Description of spatial meshes for convergence runs.

Name	Total number of cells	Hexahedrons	Tetrahedrons	Prisms	Pyramids
Mesh 1	53546	3840	28214	21212	280
Mesh 2	54900	54900	0	0	0

The solution of the nonlinear problem with pressure ration $p_1/p_2=2$ is computed for $\nu_0=1$ using the linear distribution of pressure in the tube as the initial guess. The calculation is run on 128 cores. Figs. 8-9 show the behaviour of the scaled L_0 residual $e=E_0^n/E_0^1$ as function of the time step number n for both meshes. It is seen that the use of $CFL=10$ results in a significant acceleration of the convergence as compared to both explicit run (CFL=0.25) and implicit run with a lower CFL=1. The residual does not drop below certain value due to the round-off errors associated with single-precision data. The use of the explicit method is generally very inefficient.

The second set of calculations demonstrates the scalability of the method using the hexahedral mesh 2 from Table 2. First, the so-called strong scaling test is performed in which the problem size is fixed by using the same velocity mesh of 16^3 cells. Fig. 10 shows the speed up of the calculations as function of the CPU core used relative to the performance on 16 cores. Both linearised and nonlinear equations are solved. The corresponding number are provided in Table 3. It is seen that the parallel efficiency is around 85%. On 512 cores the largest communication overhead is associated with the calculation

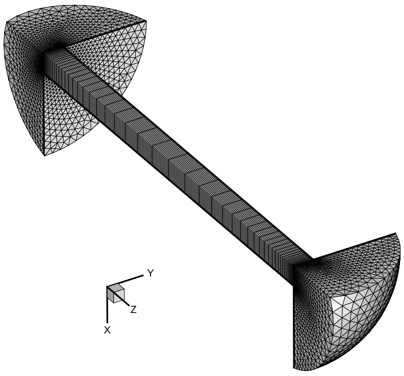

Figure 4: Mixed-element mesh 1 from Table 2.

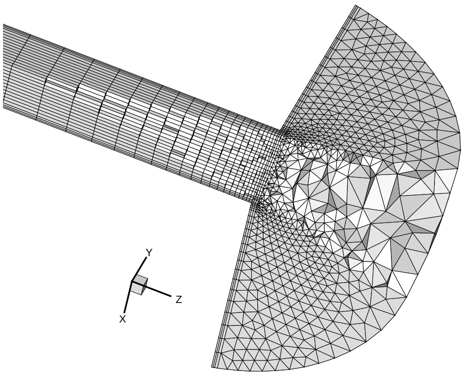

Figure 5: Cross-sectional view of the mesh from Fig. 4.

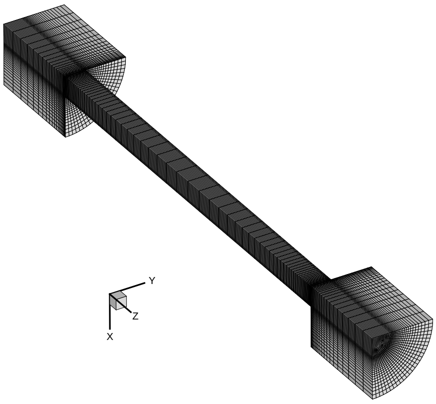

Figure 6: Purely hexahedral mesh 2 from Table 2.

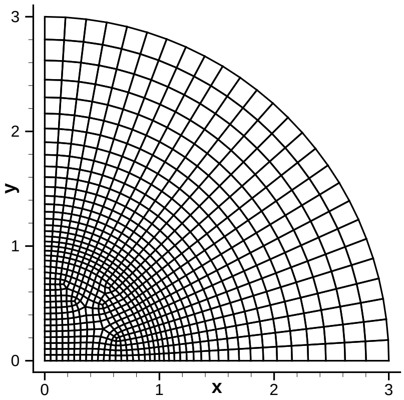

Figure 7: Cross-sectional view of the mesh from Fig. 6.

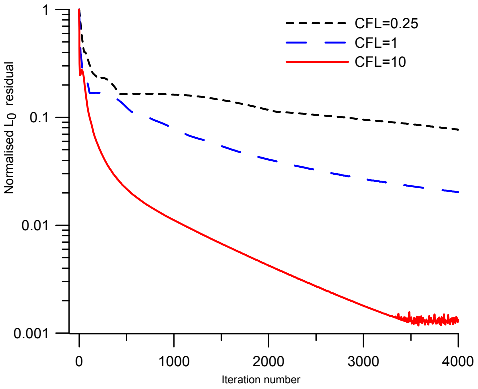

Figure 8: Convergence history for mixed-element Mesh 1 from Table 2.

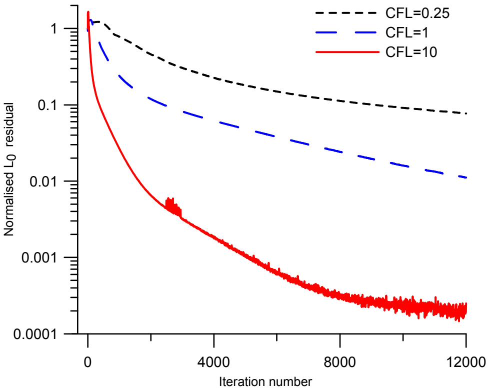

Figure 9: Convergence history for hexahedral Mesh 2 from Table 2.

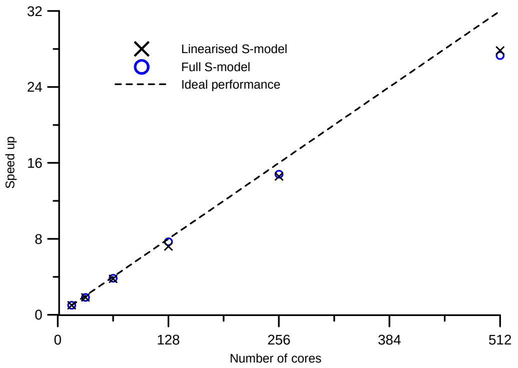

Figure 10: Strong scalability of the method relative to the 16-core run on the spatial mesh of 5×10^4 cells and molecular velocity mesh of 16^3 cells.

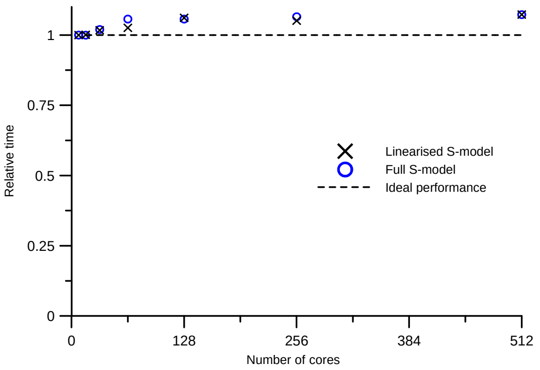

Figure 11: Weal scalability of the method relative to the 16-core run on the spatial mesh of 5×10^4 cells and molecular velocity mesh of 16^3 cells.

Table 3: Speed up for the strong scaling analysis.

Number of cores	16	32	64	128	256	512
Linearized equation	1.	1.83	3.79	7.20	14.58	27.85
Nonlinear equation	1.	1.83	3.85	7.70	14.81	27.31

Table 4: Relative computing times for the weak scaling analysis.

Number of cores	8	16	32	64	128	256	512
Linearized equation	1.	1.00	1.02	1.03	1.06	1.05	1.07
Nonlinear equation	1.	1.00	1.02	1.06	1.06	1.07	1.07

of macroscopic parameters and accounts for 10% of computational cost. Other communication overheads are below 1% of the computational cost of the time step.

Next, the weak scaling of the method and the code was studied by increasing the problem size with the increasing number of cores. The reference point in the study is the 8-core run on the molecular velocity mesh with $16^2\times12=3072$ cells. The size of the velocity mesh is then doubled with increasing the number of cores so that on 512 cores it is equal to $\approx2\times10^5$ cells. Fig. 11 shows the computing times relative to the 8-core run. The corresponding numerical values are provided in Table 4. The efficiency of the method in this case is above 90%. On 512 cores the largest communication overhead is associated with the calculation of macroscopic parameters and accounts for 5% of computational cost.

Overall, the parallel efficiency of the method is very good up to 512 cores. The weak scaling would be important for hypersonic blunt-body calculations which require very large velocity meshes. For the slow micro-scale flows the strong scaling is more crucial as the velocity mesh is generally not very fine, but the spatial mesh needs to be quite large.

4.2 Mass flow rate calculations

The main computed integral characteristic of the flow is the non-dimensional mass flow rate M, given by the formula (2.8) for the nonlinear model equation and (2.14). In order to cancel out the influence of the pressure ratio and channel's length, the computational results are given in terms of the normalized mass flow rate M_p

$$M_p = -\frac{2l}{\Delta P} M. \tag{4.1}$$

Eq. (4.1) is similar to the formula (2.16) for M_{Pois} in that the mean pressure gradient $\Delta P/(2l)$ resembles the imposed pressure gradient K_P in the flow model (2.15).

For the main set of calculations three significantly finer meshes were considered, the parameters of which were selected according to the following considerations. For the fixed micro channel length the main flow parameter affecting the accuracy is the rarefaction parameter ν_0 (or Knudsen number Kn). For $\nu_0 \ll 1$ the distribution function is discontinuous. The discontinuities originate from the exits of the channel ($z = \pm l$) and propagate both inside the channel and into the reservoirs. Moreover, the distribution function varies rapidly around $\boldsymbol{\xi} = 0$. In order to account for these factors, a rather fine molecular velocity mesh with clustering towards the origin is required. The spatial mesh needs to be fine enough along the channel, but does not need to be refined towards its surface. The opposite regime is a nearly continuum flow $\nu_0 \gg 1$, which requires a second-order accurate spatial discretisation scheme and a relatively fine spatial mesh; the molecular velocity resolution can be course (typically with $\Delta\xi \approx 0.4$) as long as a conservative integration procedure is used. For intermediate values $0.1 \leq \nu_0 \leq 5$ the resolution of both meshes need to be carefully controlled.

In calculations, for $\nu_0 \leq 1$ the spatial mesh contained 95200 hexahedral cells and was constructed from the coarse mesh 2 used in the previous section by refining the resolution in the z coordinate direction inside the channel. The molecular velocity mesh consisted of 32^3 cells so that $\Delta\xi \approx 0.07$ near the origin. For $\nu_0 \geq 5$ two much finer spatial mesh were used with cells clustering towards the surface of the channel; cell size normal to the surface is ≈ 0.005. The first of these meshes contained 366240 cells hexahedral cells where the second, finer, mesh consist of $N_{space} = 513520$ cells, of which there were 206000 hexahedral in the near-surface layer and reservoirs and 307520 prismatic cells inside the channel.. In the molecular velocity space a uniform mesh was used with 12^3 cells for the linearised calculations and 16^3 cells for the nonlinear kinetic model runs.

Most of the calculations have been run on 128 cores. For the nonlinear kinetic model one time step of the algorithm requires approximately 100 seconds of computer time for the first mesh ($N_{space} = 95200$, $N_\xi = 32^3$) and around 50-55 seconds for the second mesh ($N_{space} = 513520$, $N_\xi = 16^3$). The variation in the computing time for the second mesh is due to the varying number of Newton iterations in the calculation of the macroscopic quantities: larger values of ν_0 in general require more iterations and thus incur more communication overheads between cores and thus larger computational times.

Table 5: Normalized mass flow rate M_p.

ν_0	0	0.01	0.1	0.2	0.5	1	5	10	20
Linearized	1.2357	1.2326	1.2178	1.2167	1.2441	1.3151	2.1356	3.2293	5.3817
$p_1/p_2=1.1$	1.2335	1.2331	1.2208	1.2144	1.2401	1.3179	2.1537	3.2201	5.3370
$p_1/p_2=2$	1.2343	1.2347	1.2220	1.2165	1.2421	1.3183	2.1246	3.2091	5.2102

Table 5 contains the computed values of the normalized flux M_p for both linearised and nonlinear solutions for the whole range of the constant collision frequency (rarefaction parameter) ν_0 (and hence the Knudsen number Kn). The corresponding curves can be found in Fig. 12. It is seen that for considered ratio of the length to diameter of the microchannel the mass flow rate curves have a weak minimum, called the Knudsen minimum, which is located around $\nu_0 \approx 0.2$. There is overall a very good agreement between the solutions for various pressure ratios for $\nu_0 \leq 10$. For the largest $\nu_0 = 20$ the calculated M_p for $p_1/p_2 = 2$ diverges somewhat from the linearised solution and nonlinear solution for $p_1/p_2 = 1.1$; however, the 2% difference is within the numerical error.

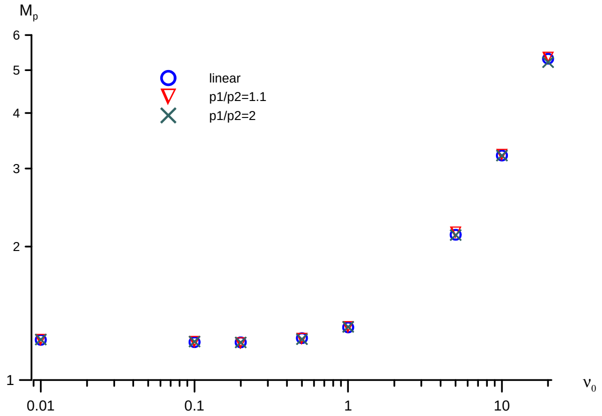

Figure 12: Comparison of M_p for linearised and non-linear kinetic models for various pressure jump values.

4.3 Comparison with the asymptotic solution

Table 6 provides the comparison of the three-dimensional solution of the linearised equation (2.11) with the Poiseuille solution (2.15) taken from [51]. The corresponding graphical illustration is found in Fig. 13. It is evident from Fig. 13 that the agreement is quite poor and the curves only approach each other for $\nu_0 \geq 10$. There are three reasons for the observed disagreement. Firstly, the present length to diameter ratio of $l/a = 10$ may not be sufficiently large for the three-dimensional solution to agree well with the asymptotic Poiseuille computation. The error is expected to be proportional to $a/l \approx 10\%$. Secondly, the considered computational meshes are quite coarse and thus the numerical error may still be not negligible. It is suffice to say that in the Poiseuille calculations [51] the spatial

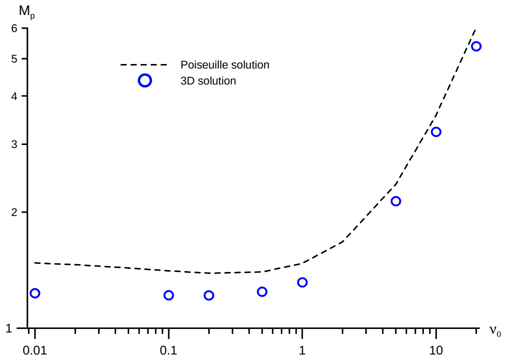

Figure 13: Comparison of M_p for linearised 3D and asymptotic 2D solutions.

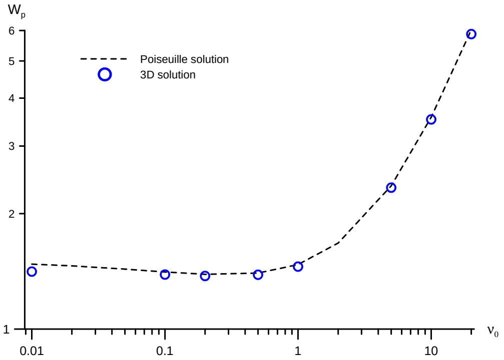

Figure 14: Comparison of pressure-gradient scaled values W_p for linearised 3D and asymptotic 2D solutions.

Table 6: Comparison of the coefficient M_p from (2.8) with the Poiseuille solution from [51].

ν_0	0	0.01	0.1	0.2	0.5	1	5	10	20
M_p	1.2357	1.2326	1.2178	1.2167	1.2441	1.3151	2.1356	3.2293	5.3817
$M_{\rm Pois}$	1.5023	1.4765	1.4085	1.3893	1.3998	1.4731	2.3619	3.5674	6.0207

Table 7: Comparison of the coefficient W_p from (4.2) with the Poiseuille solution from [51].

ν_0	0	0.01	0.1	0.2	0.5	1	5	10	20
W_p	1.4164	1.4123	1.3872	1.3754	1.3854	1.4549	2.3369	3.5193	5.8726
$M_{\rm Pois}$	1.5023	1.4765	1.4085	1.3893	1.3998	1.4731	2.3619	3.5674	6.0207

mesh contained several times more cells than the two-dimensional mesh for the cross section of the microchannel in the present work. Perhaps, the most important observation is that the actual pressure gradient in the middle section of the finite-length channel is different from $\Delta P/2l$ due to the end effects caused by the finite length of the channel and has to be found in calculations. As will be shown later, the pressure gradient along the channel is constant in the large part of the channel $|z| \le l - \delta l$, but varies in all three coordinate directions near its ends $z = \pm l$.

Following the idea from [39,40], it is more appropriate to compare the Poiseuille data with the mass rate from the linearised three-dimensional calculation normalized by the actual (calculated) pressure gradient in the middle section of the channel

$$W_p = -\frac{1}{d\hat{p}/dx}\hat{M}. \tag{4.2}$$

The results are presented in Table 6 and in Fig. 14. It is seen that there is an excellent agreement between two solutions in the range $0.1 \le \nu_0 \le 10$. The disagreement for smaller ν_0 (nearly free-molecular regime) is expected [39,40] as the Poiseuille solution becomes invalid for $(l/a)\nu_0 = \mathcal{O}(1)$. The small (around 2%) divergence of the results for $\nu_0 = 20$

may be due to both the insufficient resolution of the three-dimensional spatial mesh and the effects of the finite channel length.

Overall, Table 6 and Fig. 14 demonstrate that the three-dimensional linearised solution exhibits linear dependence of the mass flow rate on the pressure gradient in the middle of the channel. For the non-linear calculations with the finite pressure ratio the similar comparison is difficult, if not impossible, to be made because both pressure gradient and collision frequency vary along the micro channel.

4.4 Flow field

Figs. 15-16 show distributions of the normalized pressure p'

$$p' = \frac{p - p_0}{\Delta P}$$

and scaled mass flow rate $\frac{2l}{\Delta P}\hat{w}$ for $\nu_0 = 1, 5$ and linearized flow in the cross-section of the channel in the polar coordinates r,z, where $r^2 = x^2 + y^2$. It is seen that in the large part of

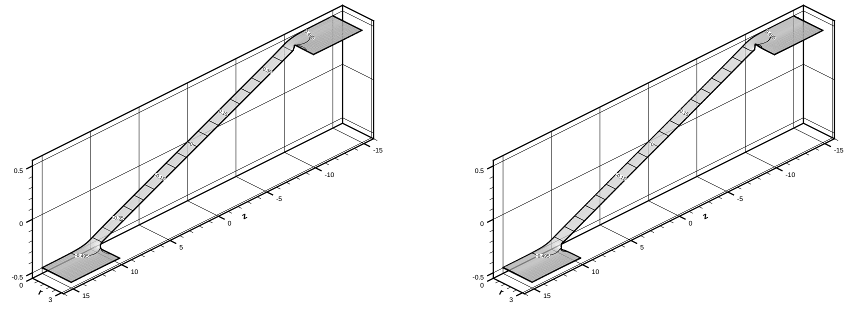

(a) $\nu_0 = 0.1$ (b) $\nu_0 = 5$

Figure 15: Normalized pressure $p' = (\hat{p} - \hat{p}_0)/\Delta P$ for different ν_0 and the linearised solution.

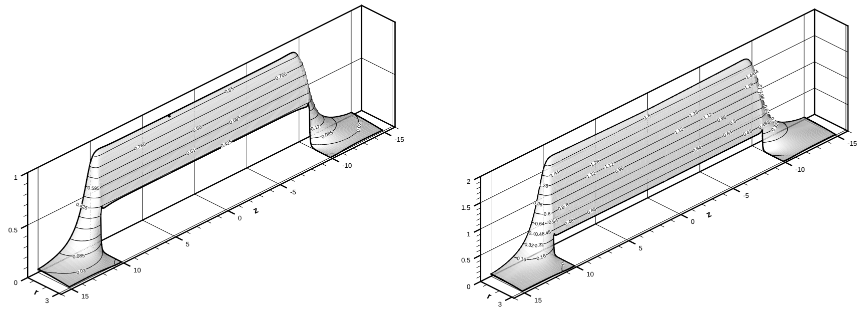

(a) $\nu_0 = 0.1$ (b) $\nu_0 = 5$

Figure 16: Normalized mass flux $(2l/\Delta P)\hat{w}$ for different ν_0 and the linearised solution.

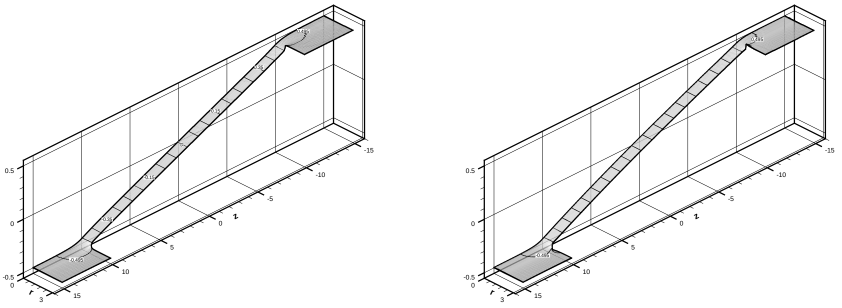

(a) $\nu_0 = 0.1$ (b) $\nu_0 = 5$

Figure 17: Normalized pressure $p' = (p - p_0)/\Delta P$ for different ν_0 and $p_1/p_2 = 2$.

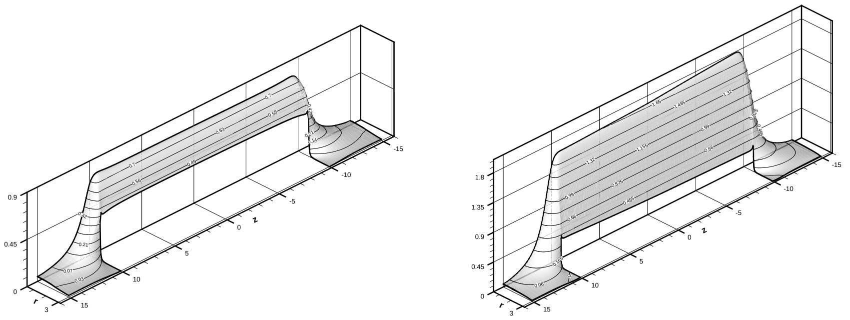

(a) $\nu_0 = 0.1$ (b) $\nu_0 = 5$

Figure 18: Normalized mass flux $(2l/\Delta P)\rho w$ for different ν_0 and $p_1/p_2 = 2$.

the micro channel the pressure gradient along the channel is constant whereas the mass flux changes only in the radial direction. The linearised temperature $\hat{T}$ does not exceed 10^{-2} in absolute value and is thus not shown. Near the ends of the channel the flow is however essentially three-dimensional.

Figs. 17-18 show distributions of the normalized pressure and scaled mass flux $\frac{2l}{\Delta P}\rho w$ for the case $p_1/p_2 = 2$ and the same values of the collision frequency $\nu_0 = 1, 5$. It is seen that the normalized pressure distributions are very similar to those in the linearised case, compare with Fig. 15. The mass flux distribution is similar to the linearised case for $\nu_0 = 0.1$ only, albeit with somewhat smaller magnitude. As ν_0 increases (Knudsen number decreases), the flow becomes nonlinear and the mass flux distribution is essentially multi-dimensional.

5 Conclusions

A numerical framework for modelling the three-dimensional steady rarefied gas flows on the basis of the Boltzmann kinetic equation with the model collision integrals has been proposed. It consists of a high-order accurate implicit discretization scheme, coupled with the conservative procedure for the calculation of the model collision integral. The application of the method to the rarefied gas flow through the finite-length circular pipe has been carried out for both weakly nonlinear (linearized) and fully non-linear flows. The results demonstrate good accuracy of the proposed algorithms across a wide range of Knudsen numbers, high efficiency of the implicit time evolution method for arbitrary unstructured meshes as well as good scalability for up to 512 cores on a modern HPC machine. Future work include the application of the method to hypersonic re-entry flows as well as extension to diatomic gases [33] and gas mixtures [1, 12].

Acknowledgments

This work was supported by the Russian Foundation for Basic Research, project no. 10-01-00721-a. The author would also like to thank Dr. Les Oswald from the IT department of Cranfield University for his help with running large-scale parallel simulations on university's HPC facility Astral and anonymous reviewers whose critical comments helped to improve the paper.

References

[1] P. Andries, K. Aoki, and B. Perthame. A consistent BGK-type model for gas mixtures. Journal of Statistical Physics, 106:993–1018, 2002.

[2] Yu.A. Anikin, Yu.Yu. Kloss, D.V. Martynov, and F.G. Tcheremissine. Computer simulation and analysis of the Knudsen experiment of the 1910 year. Journal of nano and microsystem technique, (8), 2010.

[3] K. Aoki, H. Yoshida, and T. Nakanishi. Inverted velocity profile in the cylindrical Couette flow of a rarefied gas. Physical Review E, 68(016302), 2003.

[4] V.V. Aristov and S.A. Zabelok. A deterministic method for solving the Boltzmann equation with parallel computations. Comp. Math. Math. Phys., 42(3):406–418, 2002.

[5] A. S. Arkhipov and A. M. Bishaev. Three-dimensional numerical simulation of the plasma plume from a stationary plasma thruster. Computational Mathematics and Mathematical Physics, 47(3):472–486, 2007.

[6] R. Arslanbekov, V. Kolobov, A. Frolova, and S. Zabelok. Evaluation of unified kinetic/continuum solver for computing heat flux in hypersonic blunt body flows. AIAA-2007-4544.

[7] P.L. Bhatnagar, E.P. Gross, and M. Krook. A model for collision processes in gases. I. Small amplitude processes in charged and neutral one-component systems. Phys. Rev., 94(511):1144–1161, 1954.

[8] G.A. Bird. Molecular Gas Dynamics and Direct Simulation of Gas Flows. Clarendon Press: Oxford, 1994.

[9] M. Dumbser and M. Käser. Arbitrary high order non-oscillatory finite volume schemes on unstructured meshes for linear hyperbolic systems. Journal of Computational Physics, 221(2):693–723, 2007.

[10] M. Dumbser, M. Käser, V.A. Titarev, and E.F. Toro. Quadrature-free non-oscillatory finite volume schemes on unstructured meshes for nonlinear hyperbolic systems. Journal of Computational Physics, 226:204–243, 2007.

[11] A. Frezzotti. Numerical investigation of the strong evaporation of a polyatomic gas. In Proc. 17th Symp. Rarefied Gas Dynamics, pages 1243–1250, 1991.

[12] V. Garzo, A. Santos, and J.J. Brey. A kinetic model for a multicomponent gas. Phys. Fluids, 1(2):380–383, 1988.

[13] S.K. Godunov. A finite difference method for the computation of discontinuous solutions of the equations of fluid dynamics. Mat. Sbornik, 47:357–393, 1959.

[14] M.I. Gradoboev and V.A. Rykov. Convervative method for numerical solution of the kinetic equations for small Knudsen numbers. Comp. Math. Math. Phys., 34(2):246–266, 1994.

[15] W. Gropp, E. Lusk, and A. Skjellum. Using MPI. Portable parallel programming with the message-passing interface. The MIT Press, second edition, 1999.

[16] A.V. Gusarov and I. Smurov. Gas-dynamic boundary conditions of evaporation and condensation: numerical analysis of the Knudsen layer. Phys. Fluids, 14(12):4242–4255, 2002.

[17] M.Ya. Ivanov and R.Z. Nigmatullin. Implicit scheme of S.K. Godunov with increased order of accuracy for Euler equaitons. USSR Comp. Math. Math. Phys., 27(11):1725–1735, 1987.

[18] Yu.Yu. Kloss, F.G. Cheremisin, N.I. Khokhlov, and B.A. Shurygin. Programming and modelling environment for studies of gas flows in micro- and nanostructures based on solving the Boltzmann equation. Atomic Physics, 105(4), 2008.

[19] Yu.Yu. Kloss, F.G. Cheremisin, and P.V. Shuvalov. Solution of the Boltzmann equation for unsteady flows with shock waves in narrow channels. Computational Mathematics and Mathematical Physics, 50(6), 2010.

[20] V.P. Kolgan. Application of the minimum-derivative principle in the construction of finite-difference schemes for numerical analysis of discontinuous solutions in gas dynamics. Transactions of the Central Aerohydrodynamics Institute, 3(6):68–77, 1972. in Russian.

[21] V.P. Kolgan. Application of the principle of minimizing the derivative to the construction of finite-difference schemes for computing discontinuous solutions of gas dynamics. Journal of Computational Physics, 230(7):2384–2390, 2011.

[22] V.I. Kolobov, R.R. Arslanbekov, V.V. Aristov, A.A. Frolova, and S.A. Zabelok. Unified solver for rarefied and continuum flows with adaptive mesh and algorithm refinement. J. Comp. Phys., 223:589–608, 2007.

[23] V.I. Kolobov, S.A.Bayyuk, R.R. Arslanbekov, V.V. Aristov, A.A. Frolova, and S.A. Zabelok. Construction of a unified continuum/kinetic solver for aerodynamic problems. AIAA Journal of Spacecraft and Rockets, 42(4):598, 2005.

[24] A.G. Kulikovskii, N.V. Pogorelov, and A.Yu. Semenov. Mathematical Aspects of Numerical Solution of Hyperbolic Systems. Chapman and Hall, 2002. Monographs and Surveys in Pure and Applied Mathematics, Vol. 118.

[25] I.N. Larina and V.A. Rykov. A numerical method for calculating axisymmetric rarefied gas flows. Comp. Math. Math. Phys., 38(8):1335, 1998.

[26] I.N. Larina and V.A. Rykov. Kinetic model of the Boltzmann equation for a diatomic gas with rotational degrees of freedom. Computational Mathematics and Mathematical Physics, 50(12):2118–2130, 2010.

[27] Z.-H. Li and H.-X. Zhang. Numerical investigation from rarefied flow to continuum by solving the Boltzmann model equation. International Journal for Numerical Methods in Fluids, 42(4):361–382, 2003.

[28] Z.-H. Li and H.-X. Zhang. Study on gas kinetic unified algorithm for flows from rarefied

transition to continuum. J. Comput. Phys., 193(2):708–738, 2004.

[29] I.S. Men'shov and Y. Nakamura. An implicit advection upwind splitting scheme for hypersonic air flows in thermochemical nonequilibrium. In A Collection of Technical Papers of 6th Int. Symp. on CFD, volume 2, page 815. Lake Tahoe, Nevada, 1995.

[30] I.S. Men'shov and Y. Nakamura. On implicit Godunov's method with exactly linearized numerical flux. Computers and Fluids, 29(6):595–616, 2000.

[31] L. Mieussens. Discrete velocity model and implicit scheme for the BGK equation of rarefied gas dynamics. Math. Models and Meth. Appl. Sci., 8(10):1121–1149, 2000.

[32] L. Mieussens. Discrete-velocity models and numerical schemes for the Boltzmann-BGK equation in plane and axisymmetric geometries. J. Comput. Phys., 162(2):429–466, 2000.

[33] V.A. Rykov. A model kinetic equation for a gas with rotational degrees of freedom. Fluid Dynamics, 10(6):959–966, 1975.

[34] E.M. Shakhov. Approximate kinetic equations in rarefied gas theory. Fluid Dynamics, 3(1):156–161, 1968.

[35] E.M. Shakhov. Generalization of the Krook kinetic relaxation equation. Fluid Dynamics, 3(5):142–145, 1968.

[36] E.M. Shakhov. Couette problem for the generalized Krook equation. Stress-peak effect. Fluid Dynamics, 4(5):9 – 13, 1969.

[37] E.M. Shakhov. Transverse flow of a rarefield gas around a plate. Fluid Dynamics, 7(6):961 – 966, 1972.

[38] E.M. Shakhov. Solution of axisymmetric problems of the theory of rarefied gases by the finite-difference method. USSR Comp. Math. Math. Phys., 14(4):970–981, 1974.

[39] E.M. Shakhov. Linearized two-dimensional problem of rarefied gas flow in a long channel. Computational Mathematics and Mathematical Physics, 39(7):1192–1200, 1999.

[40] E.M. Shakhov. Rarefied gas flow in a pipe of finite length. Computational Mathematics and Mathematical Physics, 40(4):618, 2000.

[41] F. Sharipov and V. Seleznev. Data on internal rarefied gas flows. J. Phys. Chem. Ref. Data, 27(3):657–706, 1998.

[42] F. Sharipov and V. Seleznev. Flows of rarefied gases in channels and microchannels. Russian Academy of Science, Ural Branch, Institute of Thermal Physics, 2008. in Russian.

[43] S. Takata, Y. Sone, and K. Aoki. Numerical analysis of a uniform flow of a rarefied gas past a sphere on the basis of the Boltzmann equaion for hard-sphere molecules. Physics of Fluids, 5(3):716–737, 1992.

[44] N.I. Tillaeva. A generalization of the modified Godunov scheme to arbitrary unstructured meshes. Transactions of the Central Aerohydrodynamics Institute, 17(2):18–26, 1986. in Russian.

[45] V.A. Titarev. Towards fully conservative numerical methods for the nonlinear model Boltzmann equation. In Preprint NI03031-NPA, page 13. Isaac Newton Institute for Mathematical Sciences, University of Cambridge, Cambridge, UK, 2003.

[46] V.A. Titarev. Conservative numerical methods for advanced model kinetic equations. In E. Onate P. Wessling and J. Periaux, editors, Proceedings of the ECCOMAS 2006. TU Delft, The Netherlands, 2006. ISBN: 90-9020970-0.

[47] V.A. Titarev. Conservative numerical methods for model kinetic equations. Computers and Fluids, 36(9):1446 – 1459, 2007.

[48] V.A. Titarev. Numerical method for computing two-dimensional unsteady rarefied gas flows in arbitrarily shaped domains. Computational Mathematics and Mathematical Physics, 49(7):1197–1211, 2009.

[49] V.A. Titarev. Implicit numerical method for computing three-dimensional rarefied gas flows using unstructured meshes. Computational Mathematics and Mathematical Physics, 50(10):1719–1733, 2010.

[50] V.A. Titarev. Implicit unstructured-mesh method for calculating Poiseuille flows of rarefied gas. Communications in Computational Physics, 8(2):427–444, 2010.

[51] V.A. Titarev and E.M. Shakhov. Nonisothermal gas flow in a long channel analyzed on the basis of the kinetic S-model. Computational Mathematics and Mathematical Physics, 50(12):2131–2144, 2010.

[52] S. Varoutis, D. Valougeorgis, and F. Sharipov. Simulation of gas flow through tubes of finite length over the whole range of rarefaction for various pressure drop ratios. J. Vac. Sci. Technol. A, 27(6):1377–1391, 2009.

[53] V. Venkatakrishnan. On the accuracy of limiters and convergence to steady-state solutions. In AIAA paper 93-0880, 31st Aerospace Science Meeting & Exhibit, January 11-14, 1993, Reno, NV, 1993.

[54] J.Y. Yang and J.C. Huang. Rarefied flow computations using nonlinear model Boltzmann equations. J. Comput. Phys., 120(2):323–339, 1995.

[55] Y.-T. Zhang and C.-W. Shu. Third order WENO scheme on three dimensional tetrahedral meshes. Communications in Computational Physics, 5(2-4):836–848, 2009.

[56] V.I. Zhuk. Spherical expansion of vapor during evaporation of a droplet. Fluid Dynamics, 11(2):251–255, 1976.